Geophysical Journal International

Geophys. J. Int. (2021) **00,** 1
Advance Access publication 2021 March 04
GJI Gravity, Geodesy and Tides

doi: 10.1093/gji/ggab088

Conditions for turbulent ekman layers in precessionally driven flow

B. A. Buffett

Department of Earth and Planetary Science, University of California, Berkeley, Berkeley, CA 94720*, USA. E-mail: bbuffett@berkeley.edu*

Accepted 2021 March 2. Received 2021 February 24; in original form 2021 January 10

SUMMARY

Ekman layers develop at the boundaries of the Earth's fluid core in response to precession. Instabilities in these layer lead to turbulence when a local Reynolds number, Re, based on the thickness of the Ekman layer, exceeds a critical value. The transition to turbulence is often assessed using experiments for steady Ekman layers, where the interior geostrophic flow is independent of time. Precessionally driven flow varies on diurnal timescales, so the transition to turbulence may occur at a different value of Re. We use 3-D numerical calculations in a local Cartesian geometry to assess the transition to turbulence in precessional flow. Calculations retain the horizontal component of the rotation vector and account for the influence of fluid stratification. The transition to turbulence in a neutrally stratified fluid occurs near $Re = 500$, which is higher than the value $Re = 150$ usually cited for steady Ekman layers. However, it is comparable to the nominal value for precessional flow in the Earth. Complications due to fluid stratification or a magnetic field can suppress the transition to turbulence, reducing the likelihood of turbulent Ekman layers in the Earth's core.

Key words: Earth rotation variations; Tides and planetary waves; Numerical modelling.

1 INTRODUCTION

Precession drives fluid motion in the Earth's liquid core (Stewartson & Roberts 1963). A large part of this motion is comprised of a rigid-body rotation relative to the overlying mantle. Viscous boundary layers (i.e. Ekman layers) form to satisfy no-slip boundary conditions. This basic flow is subject to a number of instabilities. Inertial instabilities can develop in the interior of the fluid (Kerswell 1993), and shear instabilities can occur in the Ekman layers (Lorenzani & Tilgner 2001). A quantitative assessment of the shear instabilities (Cebron *et al.* 2019) is often based on the related and well-studied case of steady Ekman layers (Deusebio *et al.* 2014), where the interior flow is independent of time. By comparison, the precessional flow varies on diurnal timescales. This means that the timescale for change in the flow is comparable to the time required to develop a steady Ekman layer. Precessional flows should still become turbulent when the velocity is large enough, but differences might be expected from predictions based on a steady Ekman layer (Caldwell & Van Atta 1970).

Linear stability of steady Ekman layers is formulated in terms of a local Reynolds number, $Re = UL_\nu/\nu$, where U is the amplitude of the interior flow, ν is the kinematic viscosity, and L_ν is the thickness of the Ekman layer (defined below). The onset of instability occurs at $Re = 55$ and takes the form of rolls that are slightly misaligned with the direction of flow (Lilly 1966). Accounting for the horizontal component of the rotation vector in Cartesian geometries causes a modest shift the critical Re, depending on the direction of flow (Leibovich & Lele 1985). Subsequent development of turbulent flow is shown by experiments to occur once $Re = 150$ (Caldwell & Van Atta 1970; Sous *et al.* 2013).

Precessionally driven flow is nominally 4 mm s^{-1} near the core–mantle boundary (Tilgner 2015), which corresponds to a local $Re \approx 500$ for a representative value of viscosity. Flow with this range of Re should become turbulent if the results of steady Ekman layers are applicable to oscillatory flows. A possible complication in the core arises from the presence of a magnetic field. The study of Desjardins *et al.* (1986) found that a radial magnetic field increases the critical value of Re by a factor of two (or less) for plausible magnetic fields. This change is probably not enough to alter our expectations of turbulence based on the steady Ekman layer. Consequently, a key question for precessional flow is whether the steady Ekman layer establishes the conditions for turbulence.

To address this question we run a series of numerical experiments in Cartesian geometries to quantify the nature of turbulence in both steady and oscillatory Ekman layers. Results for the steady Ekman layer confirm many of the well-established features of this flow. Extensions to the oscillatory Ekman layer show that the onset of instability occurs in a form similar to that for the steady case. However, turbulence does not occur until Re reaches or exceeds 500. These results suggest that precessional flow in the Earth lies close to the conditions for turbulent boundary layers. Our turbulent solutions at $Re = 500$ have viscous stresses at the boundary that are only marginally above those for the basic laminar flow. This means that turbulent Ekman layers should not substantially alter the viscous stress on the mantle. However, turbulence can be effective in mixing stratified fluid near the boundary.

We begin in Section 2 with a brief discussion of steady and oscillatory Ekman layers. We adopt a frame of reference that moves with the interior fluid so that the Ekman layer is generated by moving the solid boundary relative to a static interior. This choice greatly simplifies the numerical implementation. The numerical model is developed in Section 3 using Oceananigans.jl (Ramadhan *et al.* 2018), which is a flexible solver for incompressible fluid flow. A series of 3-D solutions for steady and oscillatory Ekman layers is presented in Section 4. We explore the role of fluid stratification in Section 5 and draw conclusions in Section 6.

2 STEADY AND OSCILLATORY EKMAN LAYERS

Ekman layers in this study are described in a local Cartesian system $[x, y, z]$, where x and y denote the eastward and northward coordinates, and z defines the vertical position. The fluid occupies the region $z \le 0$. We avoid the need to prescribe a background flow in the interior by imposing a horizontal velocity on the solid boundary at $z = 0$ above an initially static fluid. The steady and oscillatory cases are distinguished by the time dependence of this boundary condition.

In the absence of stratification the fluid velocity, $\boldsymbol{u} = [u, v, w]$, in the boundary layer is governed by (see the Appendix)

$$\frac{\partial \boldsymbol{u}}{\partial t} + \boldsymbol{u} \cdot \nabla \boldsymbol{u} + \boldsymbol{f} \times \boldsymbol{u} = -\frac{1}{\rho} \nabla P + \nu \nabla^2 \boldsymbol{u} \tag{1}$$

where P is the modified pressure and the Coriolis parameter,

$$\boldsymbol{f} = 2\Omega\,[0, \sin\theta, \cos\theta]\,, \tag{2}$$

depends on the planetary rotation rate, Ω, and the colatitude, θ, of the local Cartesian coordinate system. Solutions are also subject to the incompressibility condition $\nabla \cdot \boldsymbol{u} = 0$.

2.1 Steady Case

Steady solutions arise when the imposed boundary motion is independent of time. A solution is sought in the form

$$\boldsymbol{u} = \Re(\tilde{u}(z)[\hat{\boldsymbol{x}} + i\,\hat{\boldsymbol{y}}]) \tag{3}$$

where $\tilde{u}(z)$ describes the unknown depth-dependence and $(\hat{\boldsymbol{x}}, \hat{\boldsymbol{y}})$ define unit vectors in the coordinate directions. The horizontal components of the momentum equation in the Ekman layer represent a balance between Coriolis and viscous forces, whereas the vertical component involves the pressure gradient and the horizontal component of the Coriolis parameter. Substitution of eq. (3) into eq. (1) yields

$$\frac{\partial^2 \tilde{u}}{\partial z^2} = -i2(\Omega/\nu)\cos\theta\,\tilde{u}(z) \tag{4}$$

and

$$\frac{1}{\rho}\frac{\partial P}{\partial z} = -2\Omega \sin\theta\,\tilde{u}(z)\,. \tag{5}$$

Solutions for P (if needed) can be obtained from eq. (5) once $\tilde{u}(z)$ is computed from eq. (4). Setting $\tilde{u}(0) = U$ (a real constant) imposes a steady boundary velocity in the $\hat{\boldsymbol{x}}$ direction. The solution for $\tilde{u}(z)$ in the region $z \le 0$ becomes

$$\tilde{u}(z) = U e^{(1-i)z/L_\nu} \tag{6}$$

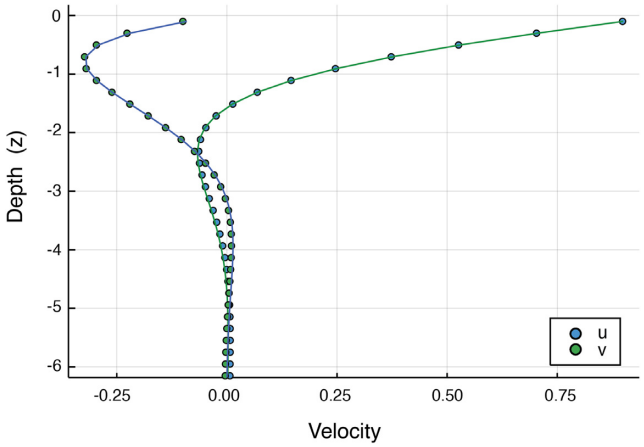

Figure 1. Velocity components u and v in a steady Ekman layer. The analytical solution (solid lines) is compared with a nearly steady-state solution from a 3-D numerical model (circles) at $Re = 25$.

where

$$L_\nu = \sqrt{\frac{\nu}{\Omega \cos\theta}} \tag{7}$$

defines the thickness of the steady Ekman layer. Individual components of the velocity are

$$[u, v, w] = U e^{z/L_\nu}[\cos(z/L_\nu),\ \sin(z/L_\nu),\ 0]\,. \tag{8}$$

A representative solution for u and v at $\cos\theta = 1$ is shown in Fig. 1. We also plot the velocities from a 3-D numerical solution of eq. (1) at $Re = 25$. A nearly steady numerical solution is established after a time interval of several rotation periods (i.e. $T = 2\pi/\Omega$).

2.2 Oscillatory Case

A large part of the fluid motion due to precession is attributed to a misalignment of the angular velocity of the core from that of the mantle. This misalignment for the case of the Earth is small (Busse 1968), which means that the relative rotation of the core can be approximated by a time-dependent vector in the equatorial plane (defined by unit vectors $\hat{\boldsymbol{X}}$ and $\hat{\boldsymbol{Y}}$). We express the relative rotation of the core in the form (Rochester *et al.* 1975)

$$\boldsymbol{\omega}_f = \Re(\,\tilde{\omega}_f[\hat{\boldsymbol{X}} + \mathrm{i}\hat{\boldsymbol{Y}}]\,e^{\mathrm{i}\Omega t}\,), \tag{9}$$

so the relative velocity of the core becomes

$$\boldsymbol{v}_f(\boldsymbol{r}, t) = \boldsymbol{\omega}_f \times \boldsymbol{r}, \tag{10}$$

where $\boldsymbol{r}$ is the position vector in a mantle-fixed frame. Expressing $\boldsymbol{v}_f$ in spherical coordinates $[r, \theta, \phi]$ gives

$$\boldsymbol{v}_f = \Re(\,\mathrm{i}\tilde{\omega}_f r[\hat{\boldsymbol{\theta}} + \mathrm{i}\cos\theta\,\hat{\boldsymbol{\phi}}]\,e^{\mathrm{i}\phi}e^{\mathrm{i}\Omega t}\,) \tag{11}$$

where $[\hat{\boldsymbol{r}}, \hat{\boldsymbol{\theta}}, \hat{\boldsymbol{\phi}}]$ define the coordinate basis vectors. A conversion of $\boldsymbol{v}_f$ to our local Cartesian system is done by letting $\hat{\boldsymbol{x}} = \hat{\boldsymbol{\phi}}$ and $\hat{\boldsymbol{y}} = -\hat{\boldsymbol{\theta}}$. The velocity of the mantle relative to the core is simply $-\boldsymbol{v}_f$. A nominal estimate for the amplitude of the motion at the core–mantle boundary ($r = 3480$ km) is specified by the misalignment angle $\tilde{m}_f = 1.7 \times 10^{-5}$ radian (Tilgner 2015). The amplitude of the relative rotation is $\tilde{\omega}_f = \Omega\tilde{m}_f$, and the relative velocity is roughly $U = \tilde{\omega}_f r \approx 4.3$ mm s^{-1}. Thus the boundary condition at $z = 0$ in the oscillatory case is

$$[u, v, w] = U[\cos\theta\cos\Omega(t - t_0),\ -U\sin\Omega(t - t_0),\ 0] \tag{12}$$

where t_0 makes a specific choice for the initial phase of the oscillatory motion. This motion is circular near the poles and becomes increasingly linear towards the equator (Pais & Le Mouel 2001)

A general solution for the oscillatory Ekman layer can be found in terms of (complex) velocity components $u_\pm = u \pm \mathrm{i}v$. A horizontal balance between inertia, Coriolis and viscous forces yields

$$\frac{\partial u_\pm}{\partial z^2} = \pm \mathrm{i}\frac{\Omega}{\nu}(2\cos\theta \pm 1) \tag{13}$$

so the solution for the horizontal velocity becomes

$$u_\pm(z,t) = u_\pm(0,t)\mathrm{e}^{(1\pm\mathrm{i})z/L_\nu^\pm}, \tag{14}$$

where

$$L_\nu^\pm = \sqrt{\frac{\nu}{\Omega}}\left(\frac{2}{2\cos\theta \pm 1}\right)^{1/2}. \tag{15}$$

The nominal thickness of the boundary layer is $(\nu/\Omega)^{1/2}$, although the value for L_ν^- diverges at $\theta = \pi/3$ because $2\cos\theta - 1 = 0$. (A similar divergence in L_ν^+ occurs at $\theta = 2\pi/3$). We return to this point in the discussion of the numerical solution.

3 NUMERICAL METHOD

3-D solutions of eq. (1) are computed using Oceananigans.jl (Ramadhan *et al.* 2018). The governing equations are expressed in non-dimensional form using $L_\nu = \sqrt{\nu/\Omega}$ as a length scale and U as a velocity scale. The timescale is L_ν/U and the pressure scale is ρU^2. The non-dimensional form of the momentum equation in eq. (1) becomes

$$\frac{\partial \boldsymbol{u}}{\partial t} + \boldsymbol{u}\cdot\nabla\boldsymbol{u} + 2Re^{-1}\mathbf{1}_\Omega \times \boldsymbol{u} = -\nabla P + Re^{-1}\nabla^2\boldsymbol{u}, \tag{16}$$

where $\mathbf{1}_\Omega = [0, \sin\theta, \cos\theta]$ is the unit vector in the direction of the planetary rotation axis. Solutions in a neutrally stratified fluid are entirely determined by the Reynolds number

$$Re = \frac{UL_\nu}{\nu} = \frac{U}{\sqrt{\nu\Omega}}. \tag{17}$$

Representative values for viscosity, $\nu = 10^{-6}$ m^2 s^{-1} (Ichikawa & Tsuchya 2015), and rotation rate, $\Omega = 0.7292 \times 10^{-4}$ s^{-1}, give a boundary thickness of $L_\nu = 0.11$ m. Adopting a boundary velocity of $U = 4.3$ mm s^{-1} means that the Reynolds number for precessional flow at the core–mantle boundary is $Re = 470$.

Numerical solutions are based on the finite-volume method using 96^3 cells in a domain with non-dimensional size $30 \times 30 \times 20$. (Consistent results are obtained using 64^3 cells in a $20 \times 20 \times 12.5$ domain, suggesting that the domain size is not an important factor.) Time-stepping is done using a third-order Runge–Kutta method and the advective terms are handled using a fifth-order WENO method (Shu 1998). Boundary conditions in x and y are periodic, and a stress-free condition is imposed on the lower boundary at $z = -20$. A no-slip condition at the top boundary ($z = 0$) defines the type of Ekman layer. A constant boundary velocity in the x direction defines the steady Ekman layer. An oscillatory Ekman layer is defined using the boundary conditions in eq. (12). To be specific we set $t_0 = 0$ in (12), although solutions are evolved over one or more rotation periods (defined by $T = 2\pi/\Omega$). This means that a full cycle of time-varying boundary conditions are imposed in the calculation. Extensions of the numerical model to account for the effects of fluid stratification are presented in Section 5.

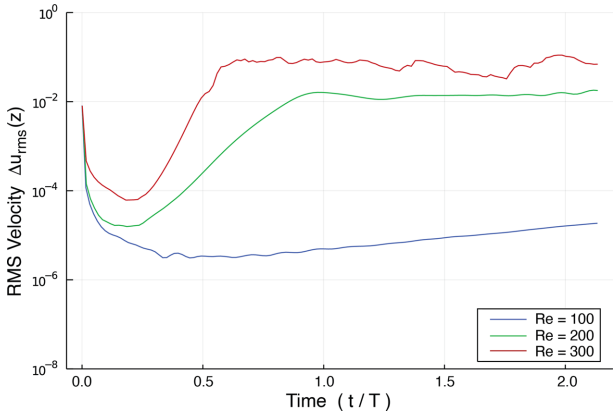

Figure 2. Root-mean-square velocity variation $\Delta u_{\mathrm{rms}}(z)$ about a horizontal average. Variations at $z = -3.2$ are plotted as a function time for several Re.

4 NUMERICAL RESULTS

We begin our discussion with the steady Ekman layer. Calculations for this case confirm several well-known features and provide a context for assessing the oscillatory Ekman layer.

4.1 Solutions for a steady Ekman Layer

We consider solutions at $Re = 100$, 200 and 300 to illustrate the transition from laminar to turbulent flow. The initial condition for each solution corresponds to a static fluid with small random fluctuations. Growth of these random fluctuations is monitored using the root-mean-square velocity variation about a horizontal average. We denote this quantity by $\Delta u_{\mathrm{rms}}(z)$ and note that it vanishes for a laminar Ekman layer. Fig. 2 shows the temporal evolution of $\Delta u_{\mathrm{rms}}(z)$ at a depth of $z = -3.2$ for the three values of Re. The initial value of $\Delta u_{\mathrm{rms}}(z)$ is set by the amplitude of the random fluctuations ($\approx 10^{-2}$), although much of this initial perturbation has spatial wavelengths that decay with time. A smaller number of unstable modes grow with time and eventually dominate the solution. Growth of the instability at $Re = 100$ is very slow and remains below 10^{-4} after two rotation periods (i.e. $t/T = 2$). On the other hand, the solution at $Re = 100$ does not decay, indicating that this Ekman layer is unstable. However, the weak growth of this instability is not sufficient to produce turbulence. By comparison, the solutions at $Re = 200$ and 300 grow more rapidly and eventually saturate before $t/T \approx 1$. Differences between the solutions at $Re = 100$ and $Re = 200$, 300 are consistent with a transition to turbulent flow at $Re = 150$.

The planform of $u(x, y, z)$ at $z = -3.2$ reveals striking differences between $Re = 100$ and 300 (see Fig. 3). Flow at $Re = 300$ exhibits strong spatial variability (Fig. 3b), whereas the motion at $Re = 100$ is close to the laminar solution (Fig. 3a). Calculating and removing the horizontal average of $u(x, y, z)$ at $z = -3.2$ reveals a wave-like feature that aligns in the direction of flow. This flow is presumably a superposition of modes that are unstable above the critical value of $Re = 55$. Consequently, the flow at $Re = 100$ may not represent a single mode of instability, but the collective properties of the unstable modes appear to account for the computed flow.

The frictional velocity, u_*, is another important property of the Ekman layer. This quantity is defined in terms of the viscous stresses at $z = 0$ according to (Tennekes & Lumley 1972)

$$|\tau| = \rho\, u_*^2, \tag{18}$$

where $|\tau|$ denotes the magnitude of the horizontal shear stress in the $\hat{\boldsymbol{x}}$ and $\hat{\boldsymbol{y}}$ directions. Fig. 4 shows the value of u_* at $Re = 300$,

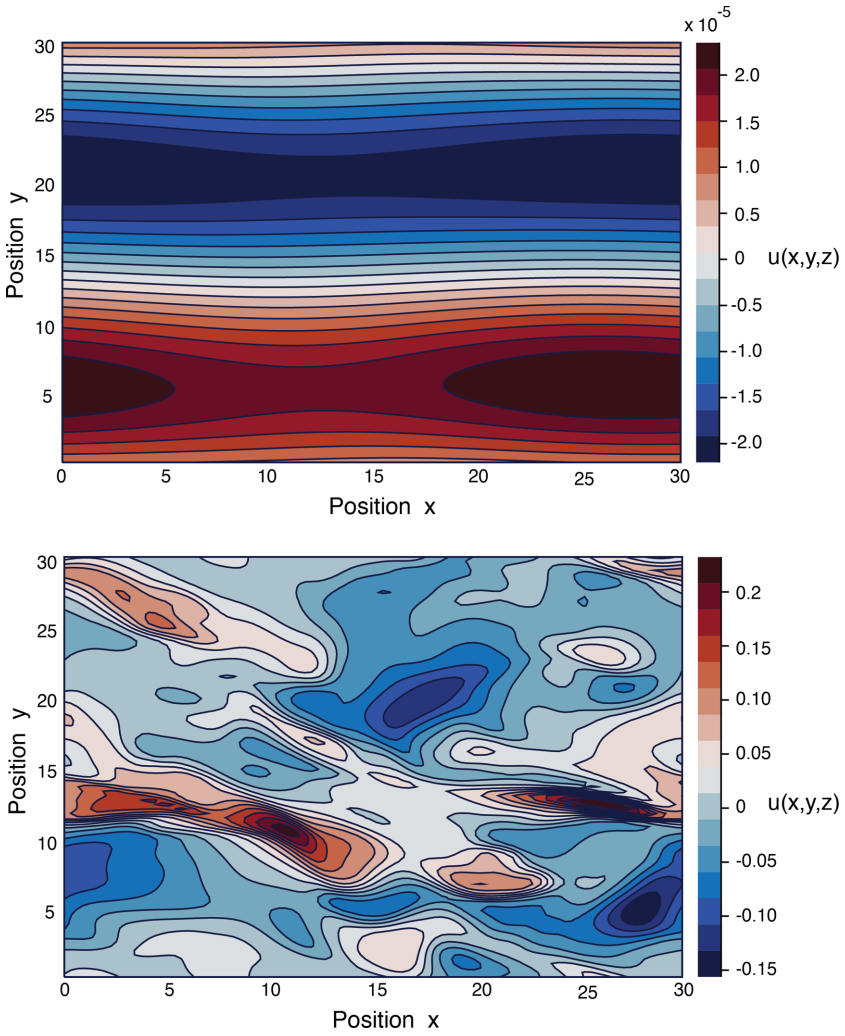

Figure 3. Eastward velocity $u(x, y, z)$ in a steady Ekman layer at a depth of $z = -3.2$. (a) The variation in u about a horizontal average at $Re = 100$ reveals a wave-like disturbance in the direction of the imposed boundary velocity. (b) The variation in $u(x, y, z)$ at $Re = 300$ shows a spatially complex flow.

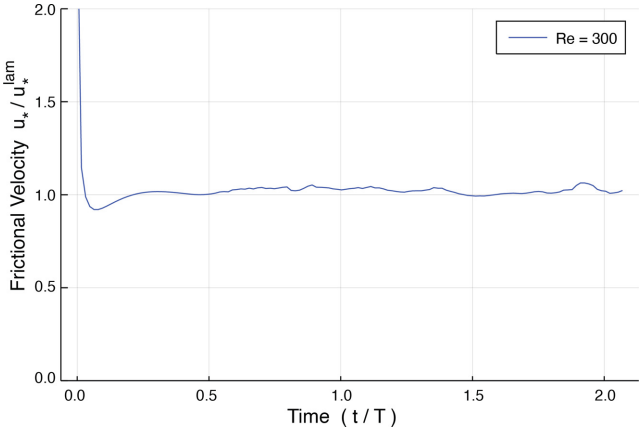

Figure 4. Frictional velocity u_* as a function of time for $Re = 300$. The numerical solution for u_* is normalized by the frictional velocity for a laminar flow.

normalized by the frictional velocity for laminar flow

$$u_*^{\rm lam} = 2^{1/4} Re^{-1/2} u(0)\,. \tag{19}$$

Large stresses at early times are due to the transient associated with a static initial condition. Once the turbulent flow evolves into a statistical steady-state we see fluctuations in u_* slightly above the laminar value. We conclude that turbulence at $Re = 300$ does not substantially alter the stress on the solid boundary.

Another quantity of interest is the depth of the turbulent Ekman layer (denoted by $L_{\rm t}$). Dimensional arguments suggest (Blackadar & Tennekes 1968)

$$L_{\rm t} \approx \frac{u_*}{f_z} \tag{20}$$

where $f_z = 2\Omega\cos\theta$ is the vertical component of $\boldsymbol{f}$. Noting that $u_* \approx u_*^{\rm lam}$ at $Re = 300$ we have

$$L_{\rm t} \approx \left(\frac{Re}{2^{3/2}}\right)^{1/2} L_\nu \tag{21}$$

when $\cos\theta = 1$. This means that $L_t \approx 10 L_\nu$ at $Re = 300$. By comparison, the vertical flow $w(x, y, z)$ at $Re = 300$ is mainly confined to a region above $z = -8$ (see Fig. 5). This result suggests that the depth of the turbulent layer is somewhat smaller than u_*/f_z; a better estimate is $L_{\rm t} = 0.8\, u_*/f_z$.

All of the results in Figs 2–5 have been computed without a horizontal component in $\boldsymbol{f}$. The neglect of f_y is usually justified when

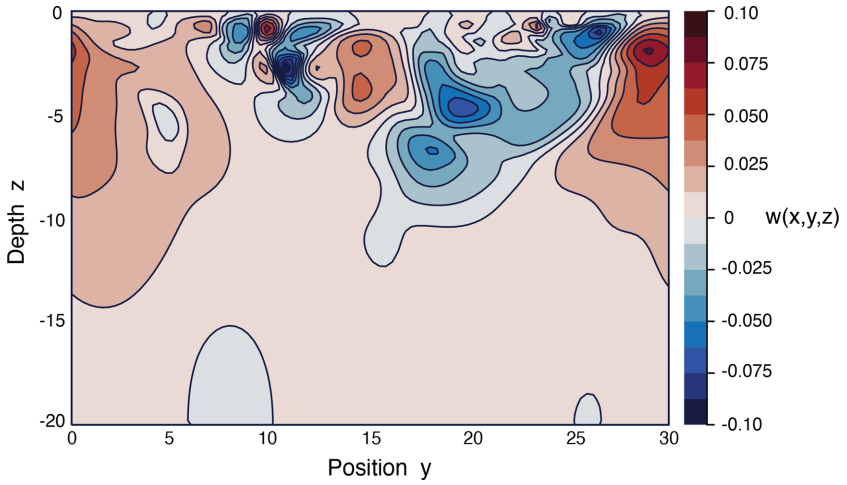

Figure 5. Turbulent vertical flow $w(x, y, z)$ in a steady Ekman layer at $Re = 300$. Most of the turbulent flow in a $y - z$ cross-section is confined to a region above $z = -8$.

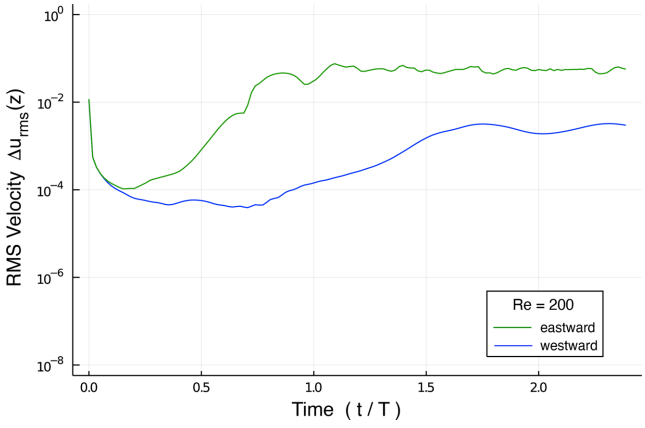

Figure 6. RMS variation $\Delta u_{\rm rms}(z)$ in a steady Ekman layer at mid-latitude $\theta = \pi/4$. The growth of instabilities at $Re = 200$ depends on the direction of flow when the horizontal component of the rotation vector is retained in the calculation. Eastward flow in the core corresponds to a negative boundary velocity.

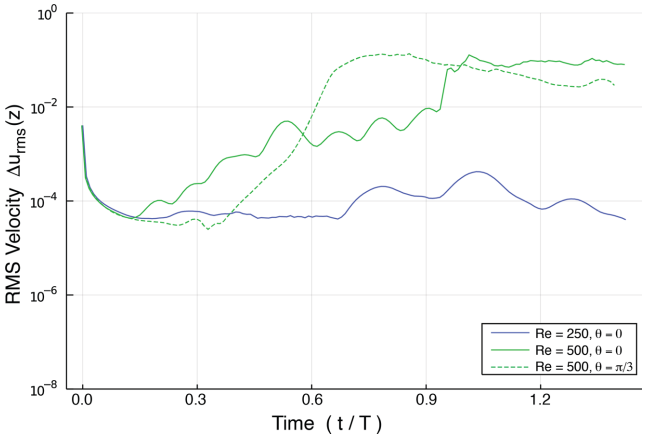

Figure 7. Evolution of velocity variation $\Delta u_{\rm rms}(z)$ in an oscillatory Ekman layer. The value of $\Delta u_{\rm rms}(z)$ is evaluated at $z = -3.2$ for several choices of Re and colatitude θ. The Ekman layers at $Re = 500$ become turbulent after an initial transient, whereas the Ekman layer at $Re = 250$ exhibits low-amplitude oscillations.

the vertical extent of flow is small compared to the horizontal dimensions. This approximation is valid for the laminar Ekman layer, but it ceases to be true once instabilities develop. The horizontal scale of the instability is comparable to the vertical scale (Leibovich & Lele 1985), so the conventional arguments do not apply. One consequence of including f_y in the dynamics is that the instability depends on the direction of flow. Fig. 6 shows the evolution of $\Delta u_{\rm rms}$ at $Re = 200$ and $z = -3.2$ for positive and negative values of U. Positive/negative boundary velocities are equivalent to westward/eastward flows in the core. Eastward flow produces a faster growth rate in $\Delta u_{\rm rms}$ and a higher value once the flow equilibrates. Conversely, westward flow has a slower growth rate for $\Delta u_{\rm rms}$ and a lower level of saturation. Calculations for $\Delta u_{\rm rms}(z)$ with $\cos\theta = 1$ and $f_y = 0$ are intermediate between these two results.

4.2 Solutions for an Oscillatory Ekman Layer

Instabilities in an oscillatory Ekman layer have a form similar to those in a steady Ekman layer. However, the value of Re for the transition to turbulence appears to be different. The evolution of $\Delta u_{\rm rms}(z)$ at $z = -3.2$ for $Re = 250$ (and $\theta = 0$) exhibits low-amplitude oscillations (see Fig. 7). By comparison, the solution at $Re = 500$ exhibits turbulent fluctuations in $\Delta u_{\rm rms}$ around a value of roughly 10^{-1}. Only small differences in the amplitude of $\Delta u_{\rm rms}(z)$ are recovered for $\theta = 0$ and $\theta = \pi/3$ after the initial transient. There is also a hint of a small modulation in the turbulent amplitude of $\Delta u_{\rm rms}(z)$ for $\theta = \pi/3$ due to changes in the amplitude of the boundary flow over a cycle.

Differences in the solutions at $Re = 250$ and 500 are also evident from the planform of $u(x, y, z)$ at $z = -3.2$ (see Fig. 8). The solution for $u(x, y, z)$ at $Re = 250$ has the form of rolls with a time-dependent orientation. By comparison the solution at $Re = 500$ is more disordered. Differences are also apparent in the friction velocity u_*. Here we normalize the frictional velocity by the laminar value for precessional flow at $\theta = 0$,

$$u_*^{\rm lam} = Re^{-1/2} u(0)\,. \tag{22}$$

The solution for u_* at $Re = 250$ is very close the laminar value after an initial transient (Fig. 9). By comparison u_* at $Re = 500$ jumps to $1.2u_*^{\rm lam}$ after the onset of turbulence. The usual definition of the

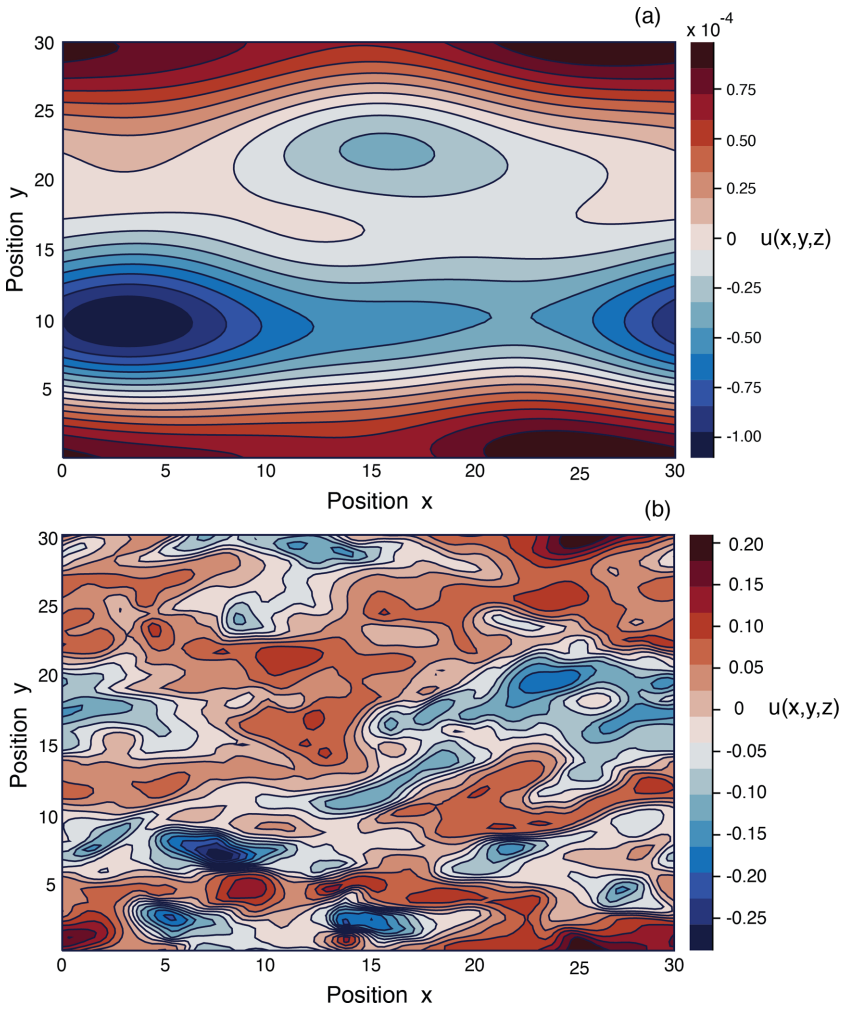

Figure 8. Eastward velocity $u(x, y, z)$ in an oscillatory Ekman layer at $z = -3.2$. (a) The solution at $Re = 250$ exhibits low-amplitude oscillations. (b) The solution at $Re = 500$ is turbulent.

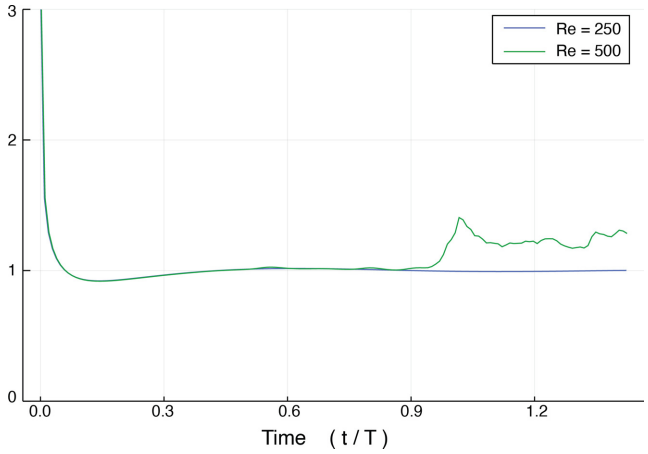

Figure 9. Frictional velocity u_* in an oscillatory Ekman layer as a function of time. Solutions are normalized by the laminar value of u_*. The solution at $Re = 500$ shows only a modest increase in friction after the onset of turbulence.

boundary-layer thickness,

$$L_t \approx \frac{u_*}{f_z} \approx \left(\frac{1.2}{2}\right) Re^{1/2} L_\nu \,, \tag{23}$$

yields $L_t = 13 L_\nu$. Our numerical solution for $w(x, y, z)$ at $Re = 500$ and $\theta = 0$ (see Fig. 10) reveals that flow is mainly confined to the region above $z = -10$, although a weak flow persists below this depth. The depth of the turbulent flow at $\theta = \pi/3$ is broadly similar. Consequently the active part of the turbulent layer is confined to a layer with a thickness of roughly $0.8 u_*/f_z$.

There is no vestige in the numerical solution of a divergence in the laminar boundary-layer thickness when $\theta = \pi/3$. Viscous stresses for $\theta = \pi/3$ are smaller than those for $\theta = 0$, but this is partly due a lower boundary velocity over part of the cycle. Normalizing the gradients $\partial u/\partial z$ and $\partial v/\partial z$ by the respective boundary velocities defines an effective length scale that differs by only 20 per cent between $\theta = \pi/3$ and $\theta = 0$. It is likely that divergent boundary layers do not develop in a transient numerical solution. While a laminar viscous layer grows into the underlying fluid at early times, the onset of turbulence alters the character of the Ekman layer. The additional complexity in the governing equations prevents the solution from reaching the long-time, laminar solution in eq. (15).

Boundary-layer instabilities in precessional flow have previously been reported by Lorenzani & Tilgner (2001). Their numerical calculations revealed instabilities above a nominal value of Re. Because these authors adopted a boundary-layer thickness of $1.4 L_\nu$, their critical value for Re in our notation is ≈140. It is likely that

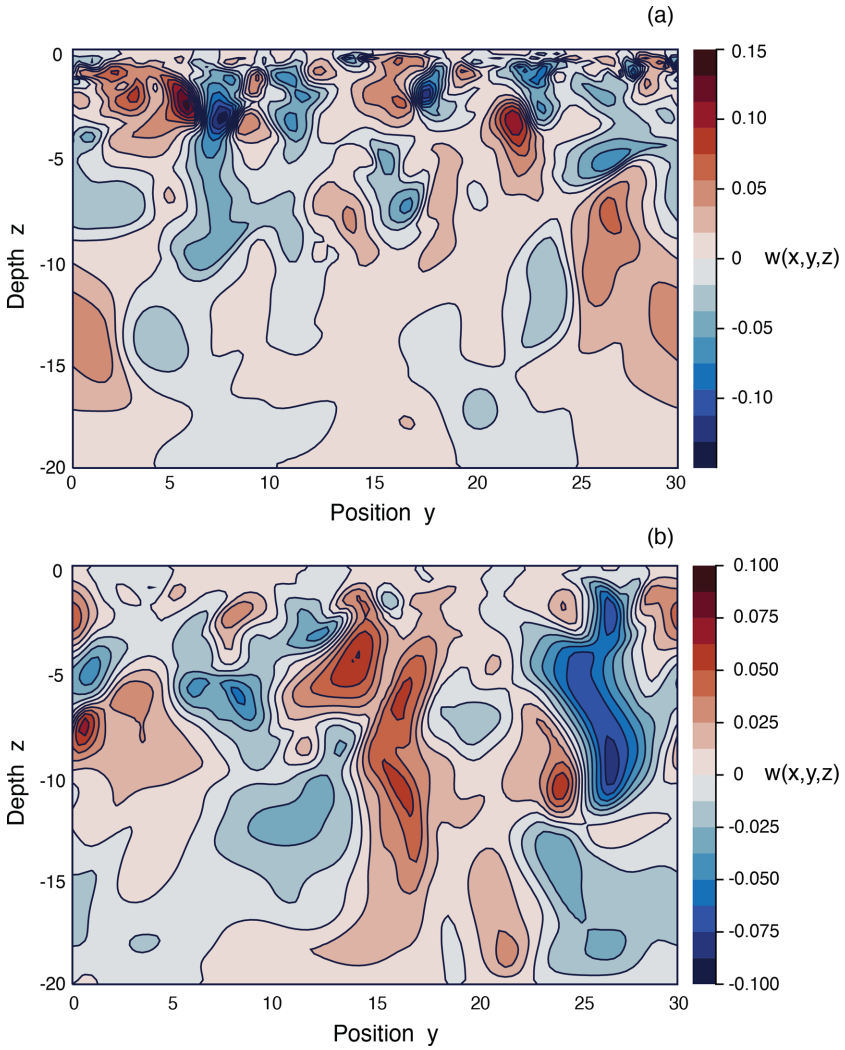

Figure 10. Turbulent vertical velocity $w(x, y, z)$ at $Re = 500$ in a y–z cross-section. Solutions at (a) $\theta = 0$ and (b) $\theta = \pi/3$ are broadly similar in amplitude. Weaker vertical flow persists below $z = -10$.

these instabilities represent wave-like features (analogous to our solution at $Re = 250$). A peak vertical flow was reported at a depth of $1.4L_v$, which is close to the depth of the maximum vertical flow ($\approx 2L_v$) in our calculation at $Re = 250$. Moreover the depth of the peak vertical flow in Lorenzani & Tilgner (2001) was nearly uniform over the boundary. Our results at $Re = 500$ suggest that a turbulent boundary layer is deeper than $1.4L_v$. Moreover, we expect large local variations in the amplitude of $w(x, y, z)$. We conclude that Ekman-layer instabilities are likely in the Earth's core, but the nominal value of $Re = 500$ for the precessional flow appears to be just large enough to permit a transition to turbulence.

5 INFLUENCE OF STRATIFICATION

Fluid stratification suppresses turbulence by restricting vertical flow (Wei & Tilgner 2013). We account for the influence of stratification by adding buoyancy effects to the momentum equation in eq. (1). The buoyancy term for the influence of density perturbations, $\Delta\rho$, is

$$\boldsymbol{F}_b = \frac{\Delta\rho}{\rho(z_0)}\boldsymbol{g} = -\frac{\Delta\rho}{\rho(z_0)} g\,\hat{\boldsymbol{z}} \equiv b\hat{\boldsymbol{z}} \tag{24}$$

where $\boldsymbol{g} = -g\hat{\boldsymbol{z}}$ is the gravity vector, $\rho(z_0)$ is the reference density and b defines the buoyancy perturbation due to motion through a background buoyancy profile

$$B(z) = -\frac{\rho(z)}{\rho(z_0)} g\,, \tag{25}$$

which is independent of time. The strength of stratification is defined by

$$\frac{\partial B}{\partial z} = N^2 \tag{26}$$

where N^2 is the (squared) buoyancy frequency.

Stratification may arise from either thermal or compositional gradients at the top of the core. The origin of stratification is not crucial for present purposes, but we do need to specify a value for the diffusivity, κ, of the buoyancy perturbation. The conservation equation for b is

$$\frac{\partial b}{\partial t} + \boldsymbol{u}\cdot\nabla(B + b) = \kappa\nabla^2 b, \tag{27}$$

which can be written in non-dimensional form using $N^2 L_v$ as a characteristic scale for B and b. (The previous choices for length and timescales also apply.) The non-dimensional equation for b

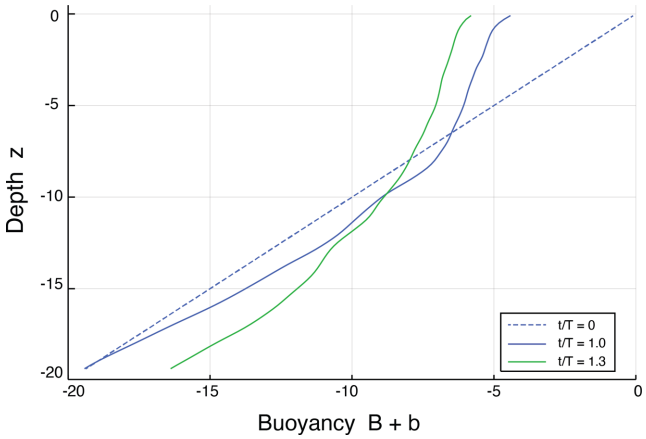

Figure 11. Vertical stratification in an oscillatory Ekman layer as a function of time. The total buoyancy $B + b$ coincides with the initial stratification $B = N^2 z$ at $t/T = 0$ because the initial perturbation b vanishes. The strength of the initial stratification is set by $N = \Omega$ and the non-dimensional solution for $B + b$ is scaled by $N^2 L_\nu$. The amplitude of boundary motion in the oscillatory Ekman layer is defined by $Re = 500$. Turbulent mixing begins in the upper part of the layer ($z > -8$) after the onset of turbulence at $t/T = 1$. Mixing continues across the entire domain at later times.

yields a single dimensionless parameter

$$Pe = \frac{U L_\nu}{\kappa} . \tag{28}$$

The corresponding non-dimensional momentum equation with buoyancy effects becomes

$$\frac{\partial \boldsymbol{u}}{\partial t} + \boldsymbol{u} \cdot \nabla \boldsymbol{u} + 2 Re^{-1} \mathbf{1}_\Omega \times \boldsymbol{u} = -\nabla P + Ri\, b \hat{\boldsymbol{z}} + Re^{-1} \nabla^2 \boldsymbol{u} \tag{29}$$

where

$$Ri = \frac{N^2}{(U/L_\nu)^2} \tag{30}$$

can be interpreted as the Richardson number.

Numerical solutions of eqs (27) and (29) are obtained using 96^3 cells in a domain with dimensions $30 \times 30 \times 20$. We let $\kappa = \nu$ and take $N = \Omega$. Periodic boundary conditions are imposed on b in the x and y directions, and no-flux conditions are imposed on b at the top and bottom boundaries. (Recall that the background stratification, $B(z)$, is independent of time.) Velocity boundary conditions are chosen to define an oscillatory Ekman layer with $Re = 500$.

Expectations for the influence of stratification are guided by the value of Ri. Introducing a dimensionless buoyancy frequency $\tilde{N} = N/\Omega$ allows us to write the Richardson number as $Ri = (\tilde{N}/Re)^2$. Our previously stated choices for $\tilde{N} = 1$ and $Re = 500$ give $Ri = 4 \times 10^{-6}$, which is small compared with the usual condition $Ri < 0.25$ for instability (Miles 1961). We expect this level of stratification to have little influence on the turbulent, and only small differences in $\Delta u_{\rm rms}(z)$ are found in the calculation relative to the neutrally stratified case. Consequently, we focus on the extent to which turbulence homogenizes the initial stratification.

Fig. 11 shows the horizontal average of the total buoyancy field, $B + b$, as a function of depth at several different times. The initial buoyancy profile at $t = 0$ is defined solely by B because the initial value of the perturbation is $b = 0$. After one rotation period ($t/T = 1$) the region above $z = -8$ has been partially mixed to produce a weaker stratification, whereas the deeper region develops a steeper buoyancy profile. Later ($t/T = 1.3$) the total buoyancy field is modified across the entire layer; values at the top and bottom of the layer are evolving towards a mean value of $B + b = -10$. Given that the overall strength of the stratification is reduced at $t/T = 1.3$, it seems likely that mixing will continue with time.

The break in the buoyancy profile at $z = -8$ and $t/T = 1$ roughly coincides with the base of the turbulent layer, as inferred from the amplitude of the vertical velocity. A weaker vertical flow persists below the nominal depth of the turbulent layer, and this flow appears to be sufficient to cause mixing. We expect this mixing to continue with time because stratification is diminished at $t/T = 1.3$, and this lowers resistance to further mixing. However, mixing cannot extend to substantially greater depths because the amplitude of $w(x, y, z)$ gradually decreases with depth. Eventually the vertical flow will be insufficient to mix the background stratification. A numerical assessment of the depth of mixing requires larger domains that retain the resolution needed to capture the viscous boundary layer.

Increasing the strength of the stratification to a value of $N = 10\Omega$ could reasonably be expected to limit the depth of mixing. Instead, the occurrence of turbulence is suppressed, even though the Richardson number is still small ($Ri = 4 \times 10^{-4}$). An oscillatory fluctuation in $\Delta u_{\rm rms}$ appears with a persistent peak value of roughly 10^{-3}. Decreasing the stratification to $N = 5\Omega$ does not change the oscillatory behaviour, although peak amplitude is slightly higher. This result can be attributed to the close proximity of $Re = 500$ to the onset of turbulence in the neutral case. Even small values for Ri are sufficient to change the nature of the solution. Setting $Re = 1000$ shifts the solution further into the turbulent regime and reduces the sensitivity to very small values of Ri. Consequently, the onset of turbulence in the Ekman layer of precessional flow with $Re \approx 500$ is liable to be sensitive to other factors, such as stratification or the presence of a magnetic field.

6 CONCLUSIONS

Ekman layers in the Earth due to precession are probably unstable (Lorenzani & Tilgner 2001), but we do not expect these layers to become fully turbulent under all possible conditions. Numerical calculations at a representative Reynolds number of $Re = 500$, based on the boundary-layer thickness L_ν, show that turbulence develops in the case of neutral stratification. The thickness of the turbulent Ekman layer at $Re = 500$ is nominally $10 L_\nu$. However, the introduction of fluid stratification can suppress the development of turbulence. A weak stratification ($N = \Omega$) appeared to have little influence on the flow relative to the neutral case, whereas a stronger stratification ($N = 10\Omega$) suppresses turbulence. Mixing in the case of weak stratification extends below the nominal depth of the turbulent layer, indicating that small-amplitude vertical motions persist below the nominal depth of the turbulent layer.

Strong sensitivity to the strength of stratification is surprising because the value of the Richardson number, Ri, is well below the usual condition for instability (i.e. $Ri < 0.25$). We attribute this sensitivity to a correspondence between the value of Re in the Earth and the value required for the transition to turbulence. A larger value for Re shifts the solution further into the turbulent regime and reduces the sensitivity to Ri. Strong stratification ($N = 10\Omega$) does not inhibit turbulent mixing at $Re = 1000$, although less mixing occurs below the base of the turbulent layer. Geophysical relevance of this result is possible with a lower value of viscosity ($\nu \approx 0.25 \times 10^{-6}$ m^{2}s^{-1}). Such a value would enable mixing of plausible stratifications in a region a few meters below the core–mantle boundary, but it would have much less influence on the

magnitude of the viscous stress. The turbulent stress is generally within a factor of two of the laminar value, even when $Re = 1000$.

ACKNOWLEDGEMENTS

This work was partially supported by the National Science Foundation EAR-1430526. The numerical calculations were enabled by the distribution of Oceananigans.jl. I thank Rich Kerswell, Jerome Noir and another knowledgeable reviewer for thoughtful comments and suggestions that improved this paper.

DATA AVAILABILITY

The numerical software used in this study is available at https://github.com/CliMA/Oceananigans.jl. Model setup and integration are defined in a set of Jupyter notebooks, which are included as an electronic supplement.

REFERENCES

Blackadar, A.K. & Tennekes, H., 1968. Asymptotic similarity in neutral barotropic planetary boundary layers, *J. Atmos. Sci.,* **25,** 1015–1020.

Busse, F. H., 1968. Steady fluid flow in a precessing spheroidal shell, *J. Fluid Mech.,* **33,** 739–751.

Caldwell, D.R. & Van Atta, C.W., 1970. Characteristics of Ekman boundary layer instabilities, *J. Fluid Mech.,* **44,** 79–95.

Cebron, D., Laguerre, R., Noir, J. & Schaeffer, N., 2019. Precessing spherical shells: flows, dissipation and the lunar core, *Geophys. J. Int.,* **219,** S34–S57.

Desjardins, B., Dormy, E. & Grenier, E., 2001. Instability of Ekman–Hartman boundary layers, with application to the fluid flow near the core–mantle boundary, *Phys. Earth Planet. Inter.,* **124,** 283–294.

Deusebio, E., Brethouwer, G., Schlatter, P. & Lindborg, E., 2014. A numerical study of the unstratified and stratified Ekman layer, *J. Fluid Mech.,* **755,** 672–704.

Ichikawa, H. & Tsuchya, T., 2015. Atomic transport properties of Fe–O liquid alloys in the Earth's outer core *P*, *T* condition, *Phys. Earth Planet. Inter.,* **247,** 27–35.

Kerswell, R. R., 1993. The instability of precession flow, *Geophys. Astrophys. Fluid Dyn.,* **72,** 107–144.

Leibovich, S. & Lele, S.K., 1985. The influence of the horizontal component of Earth's angular velocity on the instability of the Ekman layer, *J. Fluid Mech.,* **150,** 41–87.

Lilly, D. K., 1966. On the instability of Ekman boundary flow, *J. Atmos. Sci.,* **23,** 481–494.

Lorenzani, S. & Tilgner, A., 2001. Fluid instabilities in precessing spheroidal cavities, *J. Fluid Mech.,* **447,** 111–128.

Miles, J. W., 1961. On the stability of heterogeneous shear flow, *J. Fluid Mech.,* **10,** 496–508.

Noir, J., Jault, D. & Cardin, P., 2001. Numerical study of the motions within a slowly precessing sphere at low Ekman number, *J. Fluid Mech.,* **437,** 283–299.

Noir, J., Cardin, P. & Jault, D., 2003. Experimental evidence of nonlinear resonance effects between retrograde precession and the tilt-over mode with a spheroid, *Geophys. J. Int.,* **154,** 407–416.

Pais, M.A. & Le Mouel, J.L., 2001. Precession-induced flows in liquid-filled containers and in the Earth's core, *Geophys. J. Int.,* **144,** 539–554.

Ramadhan, S., *et al.*, 2018. Oceananigans.jl: Fast and friendly fluid dynamics on GPUs, *J. Open Source Softw.,* **5**(53), doi.org/10.21105/joss.02018.

Rochester, M.G., Jacobs, J.A., Smylie, D.E. & Chong, K.F., 1975. Can precession power the geomagnetic dynamo?, *Geophys. J. Int,* **43,** 661–678.

Shu, C.W., 1998. Essentially non-oscillatory and weighted non-oscillatory schemes for hyperbolic conservative laws, in *Advanced Numerical Approximation of Nonlinear Hyperbolic Equations,* Lecture Notes in Mathematics, ed. Quarteroni, A., Vol. 1697, 325–432, Springer.

Sous, D., Sommeria, J. & Boyer, D., 2013. Friction law and turbulent properties in a laboratory Ekman boundary layer, *Phys. Fluids,* **25,** 046602.

Stewartson, K. & Roberts, P.H., 1963. On the motion of a liquid in a spheroidal cavity of a precessing rigid body, *J. Fluid Mech.,* **17,** 1–20.

Tennekes, H. & Lumley, J.L., 1972. *A First Course in Turbulence,* MIT Press.

Tilgner, A., 2015. Rotational dynamics of the core, in *Treatise on Geophysics,* 2nd edn, ed. Schubert, G., **8,** 183–212, Elsevier.

Tilgner, A. & Busse, F.H., 2001. Fluid flows in precessing spherical shells, *J. Fluid Mech.,* **426,** 387–396.

Wei, X. & Tilgner, T., 2013. Stratified precessional flow in spherical geometry, *J. Fluid Mech.,* **718**(R2), 1–12.

SUPPORTING INFORMATION

Supplementary data are available at *GJI* online.

Figure OscillatoryEkman.ipynb,SteadyEkman.ipynb

Please note: Oxford University Press is not responsible for the content or functionality of any supporting materials supplied by the authors. Any queries (other than missing material) should be directed to the corresponding author for the paper.

APPENDIX: GOVERNING EQUATIONS

Several different reference frames have been used in previous studies to describe precessionally driven motion in the fluid core. The studies of Busse (1968) and Noir *et al.* (2003) adopted a frame of reference that rotates with the slow angular velocity of precession, $\mathbf{\Omega_p}$. This choice means that the angular velocities of the mantle, $\mathbf{\Omega_m}$, and the fluid core, $\mathbf{\Omega_f}$, are independent of time. Alternatively, the fluid motion can be described in a coordinate system that rotates with the mantle. In this case we need to account for changes in the orientation of $\mathbf{\Omega_m}$ due to precession. A third option (considered here) adopts a reference frame that rotates with the mean angular velocity of the fluid core (e.g. Noir et al. 2001). The angular misalignment between $\mathbf{\Omega_m}$ and $\mathbf{\Omega_f}$ is quite small ($\tilde{m}_f \approx 10^{-5}$ radian), and both of these rotation vectors precess at the same rate (Busse 1968).

It is convenient to start with the equations of motion in the mantle-fixed frame (Tilgner & Busse 2001)

$$\frac{\partial \boldsymbol{u}}{\partial t} + \boldsymbol{u}\cdot\nabla\boldsymbol{u} + 2(\mathbf{\Omega_m}+\mathbf{\Omega_p})\times\boldsymbol{u} = -\frac{1}{\rho}\nabla P + \nu\nabla^2\boldsymbol{u} \\ -(\mathbf{\Omega_p}\times\mathbf{\Omega_m})\times\mathbf{r}, \tag{A1}$$

where the Coriolis term includes a contribution from precession and the Poincaré term is added to the end of eq. (A1) to account for time variations in $\mathbf{\Omega}_m$. Solutions for flow in the interior of the core are often obtained by setting the viscous term to zero (Stewartson & Roberts 1963). This solution is possible when $|\mathbf{\Omega_p}|/|\mathbf{\Omega_m}| \approx 10^{-7}$ is much less than the flattening of the core–mantle boundary ($\epsilon_f = 2.6 \times 10^{-3}$). The resulting inviscid fluid velocity, $\boldsymbol{u_0}$, is comprised of a rigid rotation and a small correction to satisfy boundary conditions on the normal component of the velocity $\boldsymbol{u_0}\cdot\boldsymbol{n} = 0$, where $\boldsymbol{n}$ is the (outward) unit normal on the boundary. A viscous correction, $\boldsymbol{u_1}$, is added to the inviscid solution to satisfy no-slip conditions (i.e. $\boldsymbol{u_1} = -\boldsymbol{u_0}$). The equations for the viscous correction are obtained by substituting $\boldsymbol{u} = \boldsymbol{u_0} + \boldsymbol{u_1}$ into eq. (A1) and subtracting the known solution for $\boldsymbol{u_0}$, yielding

$$\frac{\partial \boldsymbol{u_1}}{\partial t} + \boldsymbol{u_1}\cdot\nabla\boldsymbol{u_0} + \boldsymbol{u_0}\cdot\nabla\boldsymbol{u_1} + \boldsymbol{u_1}\cdot\nabla\boldsymbol{u_1} + 2(\mathbf{\Omega_m}+\mathbf{\Omega_p}) \\ \times\boldsymbol{u_1} = -\frac{1}{\rho}\nabla P_1 + \nu\nabla^2\boldsymbol{u_1}, \tag{A2}$$

where P_1 is the pressure perturbation associated with $\boldsymbol{u_1}$. Steep gradients in $\boldsymbol{u_1}$ develop in the direction normal to the boundary. Because these gradients are perpendicular to $\boldsymbol{u_0}$ near the boundary we can drop the term $\boldsymbol{u_0} \cdot \nabla \boldsymbol{u_1}$ from eq. (A2). Similarly, we can drop $\boldsymbol{u_1} \cdot \nabla \boldsymbol{u_0}$ because the gradients in $\boldsymbol{u_0}$ are quite weak. The remaining nonlinear term, $\boldsymbol{u_1} \cdot \nabla \boldsymbol{u_1}$, is retained in the dynamics. Finally, we use the condition $\boldsymbol{\Omega_p} << \boldsymbol{\Omega_m}$ to obtain the governing equation in eq. (1).

One further approximation is adopted in the numerical solution. The no-slip condition at the core–mantle boundary requires $\boldsymbol{u_1} = -\boldsymbol{u_0}$. We have evaluated $\boldsymbol{u_0}$ using only the rigid rotation of the fluid core. This means that we omit the small correction associated with ellipsoidal boundaries. The relative error incurred by this omission is on the order of the flattening of the core–mantle boundary.

Key words

Authors are requested to choose key words from the list below to describe their work. The key words will be printed underneath the summary and are useful for readers and researchers. Key words should be separated by a semi-colon and listed in the order that they appear in this list. An article should contain no more than six key words.

COMPOSITION and PHYSICAL PROPERTIES
Composition and structure of the continental crust
Composition and structure of the core
Composition and structure of the mantle
Composition and structure of the oceanic crust
Composition of the planets
Creep and deformation
Defects
Elasticity and anelasticity
Electrical properties
Equations of state
Fault zone rheology
Fracture and flow
Friction
High-pressure behaviour
Magnetic properties
Microstructure
Permeability and porosity
Phase transitions
Plasticity, diffusion, and creep

GENERAL SUBJECTS
Core
Gas and hydrate systems
Geomechanics
Geomorphology
Glaciology
Heat flow
Hydrogeophysics
Hydrology
Hydrothermal systems
Infrasound
Instrumental noise
Ionosphere/atmosphere interactions
Ionosphere/magnetosphere interactions
Mantle processes
Ocean drilling
Structure of the Earth
Thermochronology
Tsunamis
Ultra-high pressure metamorphism
Ultra-high temperature metamorphism

GEODESY and GRAVITY
Acoustic-gravity waves
Earth rotation variations
Geodetic instrumentation
Geopotential theory
Global change from geodesy
Gravity anomalies and Earth structure
Loading of the Earth
Lunar and planetary geodesy and gravity
Plate motions
Radar interferometry
Reference systems
Satellite geodesy
Satellite gravity
Sea level change
Seismic cycle
Space geodetic surveys
Tides and planetary waves
Time variable gravity
Transient deformation

GEOGRAPHIC LOCATION
Africa
Antarctica
Arctic region
Asia
Atlantic Ocean
Australia
Europe
Indian Ocean
Japan
New Zealand
North America
Pacific Ocean
South America

GEOMAGNETISM and ELECTROMAGNETISM
Archaeomagnetism
Biogenic magnetic minerals
Controlled source electromagnetics (CSEM)
Dynamo: theories and simulations
Electrical anisotropy
Electrical resistivity tomography (ERT)
Electromagnetic theory
Environmental magnetism
Geomagnetic excursions
Geomagnetic induction
Ground penetrating radar
Magnetic anomalies: modelling and interpretation
Magnetic fabrics and anisotropy
Magnetic field variations through time
Magnetic mineralogy and petrology
Magnetostratigraphy
Magnetotellurics
Marine electromagnetics
Marine magnetics and palaeomagnetics
Non-linear electromagnetics
Palaeointensity
Palaeomagnetic secular variation
Palaeomagnetism
Rapid time variations
Remagnetization
Reversals: process, time scale, magnetostratigraphy
Rock and mineral magnetism
Satellite magnetics

GEOPHYSICAL METHODS
Downhole methods
Fourier analysis
Fractals and multifractals
Image processing
Instability analysis
Interferometry
Inverse theory
Joint inversion
Neural networks, fuzzy logic
Non-linear differential equations
Numerical approximations and analysis
Numerical modelling
Numerical solutions
Persistence, memory, correlations, clustering
Probabilistic forecasting
Probability distributions
Self-organization
Spatial analysis
Statistical methods
Thermobarometry
Time-series analysis
Tomography
Waveform inversion
Wavelet transform

PLANETS
Planetary interiors
Planetary volcanism

SEISMOLOGY
Acoustic properties
Body waves
Coda waves
Computational seismology
Controlled source seismology
Crustal imaging
Earthquake dynamics
Earthquake early warning
Earthquake ground motions
Earthquake hazards
Earthquake interaction, forecasting, and prediction
Earthquake monitoring and test-ban treaty verification
Earthquake source observations
Guided waves
Induced seismicity
Interface waves
Palaeoseismology
Rheology and friction of fault zones
Rotational seismology
Seismic anisotropy
Seismic attenuation
Seismic instruments
Seismic interferometry
Seismicity and tectonics
Seismic noise
Seismic tomography
Site effects
Statistical seismology
Surface waves and free oscillations
Theoretical seismology

Tsunami warning
Volcano seismology
Wave propagation
Wave scattering and diffraction

TECTONOPHYSICS
Backarc basin processes
Continental margins: convergent
Continental margins: divergent
Continental margins: transform
Continental neotectonics
Continental tectonics: compressional
Continental tectonics: extensional
Continental tectonics: strike-slip and transform
Cratons
Crustal structure
Diapirism
Dynamics: convection currents, and mantle plumes
Dynamics: gravity and tectonics
Dynamics: seismotectonics
Dynamics and mechanics of faulting
Dynamics of lithosphere and mantle
Folds and folding
Fractures, faults, and high strain deformation zones
Heat generation and transport
Hotspots
Impact phenomena
Intra-plate processes
Kinematics of crustal and mantle deformation
Large igneous provinces
Lithospheric flexure
Mechanics, theory, and modelling
Microstructures
Mid-ocean ridge processes
Neotectonics
Obduction tectonics
Oceanic hotspots and intraplate volcanism
Oceanic plateaus and microcontinents
Oceanic transform and fracture zone processes
Paleoseismology
Planetary tectonics
Rheology: crust and lithosphere
Rheology: mantle
Rheology and friction of fault zones
Sedimentary basin processes
Subduction zone processes
Submarine landslides
Submarine tectonics and volcanism
Tectonics and climatic interactions
Tectonics and landscape evolution
Transform faults
Volcanic arc processes

VOLCANOLOGY
Atmospheric effects (volcano)
Calderas
Effusive volcanism
Eruption mechanisms and flow emplacement
Experimental volcanism
Explosive volcanism
Lava rheology and morphology
Magma chamber processes
Magma genesis and partial melting
Magma migration and fragmentation
Mud volcanism
Physics and chemistry of magma bodies
Physics of magma and magma bodies
Planetary volcanism
Pluton emplacement
Remote sensing of volcanoes
Subaqueous volcanism
Tephrochronology
Volcanic gases
Volcanic hazards and risks
Volcaniclastic deposits
Volcano/climate interactions
Volcano monitoring
Volcano seismology